using statistical parametric mapping (SPM). J. Med. Invest. 52, 185–190.
Hsu, J.L., Leemans, A., Bai, C.H., Lee, C.H., Tsai, Y.F., Chiu, H.C., Chen, W.H., 2008. Gender differences and age-related white matter changes of the human brain: a diffusion tensor imaging study. Neuroimage 39, 566–577.
Hasan, K.M., Halphen, C., Boska, M.D., Narayana, P.A., 2008. Diffusion tensor metrics, T2 relaxation, and volumetry of the naturally aging human caudate nuclei in healthy young and middle-aged adults: possible implications for the neurobiology of human brain aging and disease. Magn. Reson. Med. 59, 7–13.
Hugenschmidt, C.E., Peiffer, A.M., Kraft, R.A., Casanova, R., Deibler, A.R., Burdette, J.H., Maldjian, J.A., Laurienti, P.J., 2008. Relating imaging indices of white matter integrity and volume in healthy older adults. Cereb. Cortex 18, 433–442.
Kim, J.S., Kanaan, R.A., Pearlson, G.P., 2002. Extended mutual information registration for simultaneously correcting motion effects and eddy current distortion of single-shot echo-planar diffusion tensor imaging. The Eighth International Conference on Functional Mapping of the Human Brain, Sendai, Japan.
Kochunov, P., Thompson, P.M., Lancaster, J.L., Bartzokis, G., Smith, S., Coyle, T., Royall, D.R., Laird, A., Fox, P.T., 2007. Relationship between white matter fractional anisotropy and other indices of cerebral health in normal aging: tract-based spatial statistics study of aging. Neuroimage 35, 478–487.
Le Bihan, D., 2007. The 'wet mind': water and functional neuroimaging. Phys. Med. Biol. 52, R57–R90.
Madden, D.J., Whiting, W.L., Huettel, S.A., White, L.E., MacFall, J.R., Provenzale, J.M., 2004. Diffusion tensor imaging of adult age differences in cerebral white matter: relation to response time. Neuroimage 21, 1174–1181.
Moseley, M., 2002. Diffusion tensor imaging and aging — a review. NMR Biomed. 15, 553–560.
Nusbaum, A.O., Tang, C.Y., Buchsbaum, M.S., Wei, T.C., Atlas, S. W., 2001. Regional and global changes in cerebral diffusion with normal aging. AJNR Am. J. Neuroradiol. 22, 136–142.
Ota, M., Obata, T., Akine, Y., Ito, H., Ikehira, H., Asada, T., Suhara, T., 2006. Age-related degeneration of corpus callosum measured with diffusion tensor imaging. Neuroimage 31, 1445–1452.
Ota, M., Obata, T., Akine, Y., Ito, H., Matsumoto, R., Ikehira, H., Asada, T., Suhara, T., 2007. Laterality and aging of thalamic subregions measured by diffusion tensor imaging. NeuroReport 18, 1071–1075.
Pagani, E., Agosta, F., Rocca, M.A., Caputo, D., Filippi, M., 2008. Voxel-based analysis derived from fractional anisotropy images of white matter volume changes with aging. Neuroimage 41, 657–667.
Peled, S., Gudbjartsson, H., Westin, C.F., Kikinis, R., Jolesz, F.A., 1998. Magnetic resonance imaging shows orientation and asymmetry of white matter fiber tracts. Brain Res. 780, 27–33.
Salat, D.H., Tuch, D.S., Greve, D.N., van der Kouwe, A.J.W., Hevelone, N.D., Zaleta, A.K., Rosen, B.R., Fischl, B., Corkin, S., Rosas, H.D., Dale, A.M., 2005. Age-related alterations in white matter microstructure measured by diffusion tensor imaging. Neurobiol. Aging 26, 1215–1227.
Smith, S.M., Jenkinson, M., Johansen-Berg, H., Rueckert, D., Nichols, T.E., Mackay, C.E., Watkins, K.E., Ciccarelli, O., Cader, M.Z., Matthews, P.M., Behrens, T.E.J., 2006. Tract-based spatial statistics: voxelwise analysis of multi-subject diffusion data. Neuroimage 31, 1487–1505.
Smith, S.M., Johansen-Berg, H., Jenkinson, M., Rueckert, D., Nichols, T.E., Miller, K.L., Robson, M.D., Jones, D.K., Klein, J.C., Bartsch, A.J., Behrens, T.E., 2007. Acquisition and voxelwise analysis of multi-subject diffusion data with tract-based spatial statistics. Nat. Protoc. 2, 499–503.
Snook, L., Plewes, C., Beaulieu, C., 2007. Voxel based versus region of interest analysis in diffusion tensor imaging of neurodevelopment. Neuroimage 34, 243–252.
Sullivan, E.V., Rohlfing, T., Pfefferbaum, A., 2010. Quantitative fiber tracking of lateral and interhemispheric white matter systems in normal aging: relations to timed performance. Neurobiology of Aging 31, 464–481.
Telea, A., van Wijk, J.J., 2002. An augmented Fast Marching Method for computing skeletons and centerlines. Proceedings of the symposium on Data Visualisation 2002, Barcelona, Spain, pp. 251–258.
Vernooij, M.W., de Groot, M., van der Lugt, A., Ikram, M.A., Krestin, G.P., Hofman, A., Niessen, W.J., Breteler, M.M.B., 2008. White matter atrophy and lesion formation explain the loss of structural integrity of white matter in aging. Neuroimage 43, 470–477.
Wolf-Heidegger, G., Köpf-Maier, P., 2000. Wolf-Heidegger's Atlas of Human Anatomy. Karger, Basel, New York.
Zarei, M., Johansen-Berg, H., Jenkinson, M., Ciccarelli, O., Thompson, A.J., Matthews, P.M., 2007. Two-dimensional population map of cortical connections in the human internal capsule. J. Magn. Reson. Imaging 25, 48–54.

IOP PUBLISHING PHYSICS IN MEDICINE AND BIOLOGY
Phys. Med. Biol. 55 (2010) 4119–4130 doi:10.1088/0031-9155/55/14/011

A small animal holding fixture system with positional reproducibility for longitudinal multimodal imaging

Daisuke Kokuryo, Yuichi Kimura[1], Takayuki Obata, Taiga Yamaya, Kazunori Kawamura, Ming-Rong Zhang, Iwao Kanno and Ichio Aoki

Molecular Imaging Center, National Institute of Radiological Sciences, 4-9-1 Anagawa, Inage, Chiba 263-8555, Japan

E-mail: ukimura@ieee.org

Received 13 April 2010, in final form 3 June 2010
Published 5 July 2010
Online at stacks.iop.org/PMB/55/4119

Abstract

This study presents a combined small animal holding fixture system, termed a 'bridge capsule', which provides for small animal re-fixation with positional reproducibility. This system comprises separate holding fixtures for the head and lower body and a connecting part to a gas anesthesia system. A mouse is fixed in place by the combination of a head fixture with a movable part made from polyacetal resin, a lower body fixture made from vinyl-silicone and a holder for the legs and tail. For re-fixation, a similar posture could be maintained by the same holding fixtures and a constant distance between the head and lower body fixtures is maintained. Artifacts caused by the bridge capsule system were not observed on magnetic resonance (MRI) and positron emission tomography (PET) images. The average position differences of the spinal column and the iliac body before and after re-fixation for the same modality were approximately 1.1 mm. The difference between the MRI and PET images was approximately 1.8 mm for the lower body fixture after image registration using fiducial markers. This system would be useful for longitudinal, repeated and multimodal imaging experiments requiring similar animal postures.

1. Introduction

In recent years, molecular imaging studies using multimodal approaches have become active worldwide (Weissleder and Mahmood 2001, Luker and Piwnica-Worms 2001, Massoud and Gambhir 2003, Pichler *et al* 2008). For this research, it is important to precisely acquire molecular behaviors, such as changes in disease diagnosis or brain activities. Superimposed images from anatomical and functional images provide additional information on the activities

[1] Author to whom any correspondence should be addressed.

0031-9155/10/144119+12$30.00

of tissues and molecules. In most settings, anatomical images are acquired using computed tomography (CT) or magnetic resonance imaging (MRI), while functional images are acquired using positron emission tomography (PET) or single-photon emission computed tomography (SPECT). In addition, novel functional imaging techniques that use MRI, ultrasound or optical imagers are available.

In order to obtain anatomical and functional information, or 'multimodal information', simultaneously, easily and precisely, combined multimodal imaging instruments have been developed. Some combined multimodal imaging instruments, such as PET/CT and SPECT/CT, have been developed commercially for clinical and pre-clinical uses, and instruments that use MRI and PET were developed for research. Combined instruments using MRI and PET were proposed by several research groups, and simultaneous PET and MR images have been obtained (Catana *et al* 2006, Pichler *et al* 2006, Judenhofer *et al* 2007, Gilbert *et al* 2006, Handler *et al* 2006, Yamamoto *et al* 2010). However, while the development of these combined instruments was effective for molecular imaging research, the imaging performance of each modality was decreased due to the interference from other modalities. In addition, the costs of hardware developments were substantial.

On the other hand, approaches to combine anatomical and functional information from existing modalities, such as micro CT, high-field MRI for animals, micro PET and micro SPECT, have been investigated. Their major advantage was that existing modalities could be utilized without significant modifications. Thus, the cost for improving existing modalities was much less than that for developing new hardware and there were no mechanical interferences. However, the positional offsets from moving and re-setting between multimodal imaging instruments should be addressed in order to combine anatomical and functional images. In order to use existing modalities and to precisely superimpose a functional image onto an anatomical image, holding fixtures need to be developed to maintain the same positions and postures when using different, separate modalities.

In conventional approaches, small animals were fixed in place by their forepaws, ears and hind paws using ropes, surgical tapes or ear bars (Chow *et al* 2006, Rowland *et al* 2005, Christian *et al* 2008, Woo *et al* 2009). An image chamber that included a gas anesthesia system and a removable bed for small rodents was designed, with the rodent's fore and hind paws fixed in place using strings (Chow *et al* 2006). For image registration, a three-dimensional grid phantom was filled with a contrast agent for both CT and PET imaging and used to make a spatial transformation matrix between these modalities, which was used for software registration. A head holding fixture was developed that immobilized the ears by inserting bars into the ear holes from the side for use with micro PET and MRI (Rowland *et al* 2005). With this fixture, the hind paws were immobilized using a surgical tape. Another kind of holding fixture with a hardware guidance system was proposed for PET and CT imaging (Woo *et al* 2009). For guidance, the rodent's forelimbs and hind paws were sandwiched between pins that were inserted into a bed in order to maintain the same positions. A jacket-type holding fixture has also been investigated. Christian *et al* made a holding fixture with Styrofoam® (Dow Chemical, MI, USA) and gelatin to immobilize the rodent's lower body for tumor imaging. This was compatible with CT, MRI, PET and autoradiography (Christian *et al* 2008). A mouse was placed in the immobilization device made from Styrofoam, and the gap between this device and the mouse was filled with gelatin. For image registration, four rods were embedded in this immobilization device that contained oil or a mixture of an iodine contrast agent and a radioactive tracer. However, animals should remain mounted on the fixtures for imaging by different modalities. These devices were not suitable for longitudinal experiments, such as observations of long-term changes in similar postures, or for cases when both anatomical and functional images had to be acquired on different days. The animal had to be removed after the

first scan and remounted before the next scan could be performed on another day. Therefore, the reproducibility of the positions before and after animal re-fixation to the holding fixtures could not be assumed.

The aim of this study was to develop a holding fixture with the positional reproducibility for remounting mice. In recent years, some studies on the reproducibility of proposed holding fixtures have been performed (Suckow *et al* 2009, Rommel *et al* 2008, Zhang *et al* 2008). Suckow *et al* (2009) demonstrated the positional reproducibility of Chow's imaging chamber for experiments with rodents for PET and CT imaging. The average displacement measured at bone landmarks before and after reattachment to the chamber for the entire mouse body was 1.11 mm for CT images and the average displacement without reattachment between CT and PET images was 0.23 mm. Rubber-like immobilization using alginate was used for rat experiments by Rommel *et al* (2008). The alginate molding covered the tumor area in the leg, and images before and 72 h after radiation were acquired using the same molding. The co-registration between MRI and PET images was a perfect match, which was confirmed based on the positions of external fiducial markers. Zhang *et al* (2008) proposed a repeated use rodent fixture that included a semi-cylindrical plastic cradle, an animal-specific mold using SecureFoam™ (Zanzonico *et al* 2006) and stereotactic rods to facilitate rigid body registration. A tumor-bearing leg was positioned between the rods to be placed under the templates used for registration. In addition, point markers were inserted into the tumor for image registration and for validating the reproducibility accuracy. The three-dimensional position differences at the tumor-inserted markers before and after removal from the fixture were within 0.8 mm for micro PET imaging.

For our research, a novel animal holding system was developed that included animal holding fixtures and a gas anesthesia system. This system is termed a 'bridge capsule'. To improve the positional reproducibility before and after re-fixation for longitudinal, repeated and multimodal imaging experiments with the same posture, a combination of head and lower body fixtures was developed. In this study, the designs of these fixtures are introduced. The accuracy of the reproducibility after re-fixation and multimodal image experiments for the lower body is validated using high-field MRI and micro PET imaging.

2. Materials and methods

2.1. Structure of the bridge capsule and immobilization

The structure of the bridge capsule system is shown in figure 1(a). This system comprises two separate holding fixtures for head and lower body and a connecting part to a gas anesthesia system.

The head was immobilized by placing it into the stereotactic component with a hole in the middle. This was made from polyacetal resin (DURACON®, Polyplastics Co., Ltd, Tokyo, Japan) (figures 1(b) and (c)).[2] The diameter of the front side was 31 mm and the length of the lateral side was 67 mm. This fixture had a movable part, as shown in figure 1(b). This part could be easily pulled out and returned into the fixture with an internal spring. A rod with a hook was inserted into the hole. This rod was connected to a gas anesthesia inlet. The hole had a tapered bore and the taper angle was adjusted to the skull of a mouse. A mouse's head could be easily fixed in place when the mouse's incisor was grappled by the hook and the movable part was returned (figure 1(c)).

The lower body was immobilized by a mold made from vinyl-silicone used for dental implants (EXAHIFLEX, GC Corporation, Tokyo, Japan) and a holder for the legs and tail

[2] The head part is patent pending.

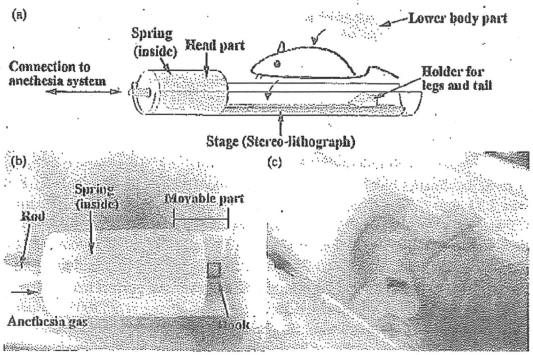

Figure 1. (a) Structure of the bridge capsule system. The system comprised two holding fixture parts for the head and lower body and a connecting part to a gas anesthesia system. (b) Head fixture and (c) fixture with a mouse. A mouse was placed in a prone position on the stage. The mouse's incisor was grappled by a hook and the movable part was returned to fix the head part using the internal spring. Anesthesia gas was supplied through the rod with a hook.

made from polyacetal resin. The vinyl-silicone was composed mostly of vinyl-polysiloxane and silica dioxide, and a mold for an individual mouse can be easily formed from it. The attenuation coefficient of the mold was 0.12 measured on an Inveon Dedicated PET Scanner (Siemens Preclinical Solutions, TN, USA). This value was obtained from a 60 min transmission scan using a ^{57}Co point source with a cylindrical phantom (diameter = 35 mm) containing vinyl-silicone and water, and the coefficient was determined with reference to the theoretical attenuation coefficient of water (0.095). A mouse was placed in the prone position on the stage made with stereo-lithography and the head was inserted into the head fixture (figure 2(a)). The tail was gently pulled, and the tail and legs were set on a holder for the legs and tail to avoid moving them during fixation (figure 2(a)). Silicone was poured onto the back of the mouse (figure 2(b)), and an acryl tube was placed on the silicone. For this vinyl-silicone, the base and catalyst paste were blended using a commercial pump dispenser (CARTRIDGE DISPENSER II, GC Corporation, Tokyo, Japan). It was hardened after about 5 min (figure 2(c)). No exothermic heat was produced during hardening. After hardening, the mold had elasticity like that of rubber, which made it easy to fit the mouse into the mold and also to remove it from the mold. Although the mold could be bent and twisted, its shape was not altered. When removing the holding fixtures, the acryl tube and the head fixture were first removed and the mouse was turned upward. Then, the holder for the legs and tail was removed from the lower body fixture, and the legs and tail were gently removed from the lower body fixture because they were embedded in the lower body mold. The prints of the legs and tail remained on the mold.

Also, a polyethylene tube (Intramedic™ Polyethylene Tubing (PE50), Becton, Dickinson and Company, NJ, USA), with a diameter of 0.58 mm, was embedded in the silicone of the lower body fixture as a fiducial marker for use in image registration (figure 2(c)). The tube was placed in a roughly horizontal direction and was folded a couple of times in order to

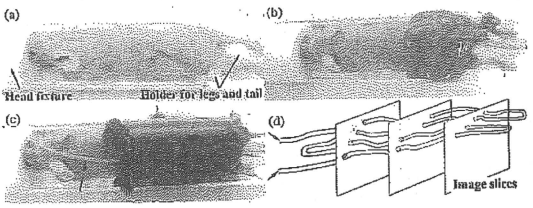

Figure 2. Construction of the lower body fixture with a mouse. (a) Mouse was placed in a prone position on the stage and the head was inserted into the head fixture and legs and tail were set in the holder made from polyacetal resin. (b) A silicone fixture to cover the lower body was molded, and (c) the silicone hardened after 5 min. The tubes (arrow) filled with a contrast agent, water and a radioisotope were embedded for image registration. (d) Schematic image of the randomized three-dimensional tube position in the lower body fixture. The positions in each image slice were different. Both ends of the tube (arrows) were connected to syringes containing a contrast agent and a radioisotope.

make it appear over three points in transverse slices to help detection of the three-dimensional position (figure 2(d)) (Humm *et al* 2003). Both ends of the tube were connected to syringes containing a contrast agent or a radioisotope.

2.2. *Re-fixation*

For longitudinal multimodal imaging with positional reproducibility, the mouse has to be re-fixed on the proposed holding fixture in order to maintain the same posture as the first scan. An anesthetized mouse was placed in the supine position in the vinyl-silicone mold (figures 3(a) and (b)). The legs and tail were set into the prints that remained when the fixture was made (figure 3(b)). After setting, the holder for the legs and tail was placed on the mouse so that they could be firmly held (figure 3(c)). Then, the mouse incisors were grappled by the hook, and the head was re-fixed in place by replacing the movable part (figure 3(d)). The distance between the head and lower body fixtures was maintained at the same value as that when fixing the lower body.

2.3. *Software-based image registration*

In order to enhance the accuracy of image registration for different modalities before and after re-fixation, a software-based approach was developed utilizing the polyethylene tube as a marker. The tube was filled with a contrast agent for MRI, such as distilled water, gadopentetate dimeglumine, or manganese, and a radioisotope for PET imaging. The registration criterion was to minimize the sum of Euclidean distances between the centroids of corresponding fiducial markers before and after re-fixation.

The procedure began by searching for the slice in an image taken after re-fixation that was similar to the neighboring slices in an image taken before re-fixation. Second, each slice after re-fixation was rotated and shifted to optimize the registration criterion. For the case of registration between the images acquired using different modalities, a lower spatial resolution was interpolated to a higher spatial resolution before registration. The lower-to-

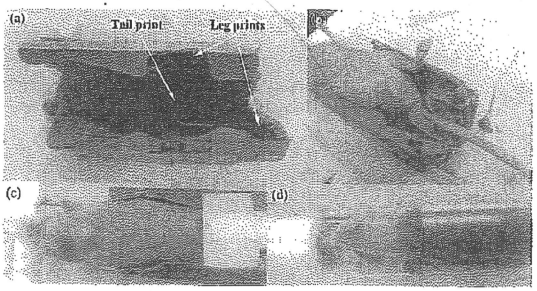

Figure 3. (a) Lower body fixture before re-fixing (backside). The prints of the legs and tail remained. (b) The tail and legs were set in the lower body fixture. (c) The holder for legs and tail was covered, and (d) the head was inserted into the head fixture. Finally, the half-cut acryl tube covered the lower body fixture.

higher approach was used because fiducial markers appearing in a high-resolution image sometimes disappeared after resampling at a low resolution.

2.4. Animal experiments and image protocol

Adult female mice (BALB/c nude, Japan SLC, Inc., Shizuoka, Japan) (19.3 ± 0.6 g, $N = 6$) were used. The mice were maintained in accordance with the guidelines of our institute, the National Institute of Radiological Sciences (NIRS), and all experiments were conducted under the approval of the NIRS Animal Protocols. The mice were anesthetized using 2.0% isoflurane gas (Escain, Mylan Co. Ltd, Tokyo, Japan). The settings for MR and PET experiments are shown in figures 4(a) and (b).

Imaging protocols for MRI and PET experiments are shown in figure 4(c). First, three sets of T_1-weighted MRI scans were conducted. The first and second scans were performed continuously, and the stability of the bridge capsule system was evaluated. The mouse was removed from the system after the second scan, and then mounted again for the third scan. The first and third scans enabled assessment of the reproducibility for animal fixation of the lower body. A few days after the MRI scans, three PET scans were performed in the same manner as the MRI scans to estimate the stability and reproducibility of PET and to compare the performances between MRI and PET.

^{1}H-MRI images were acquired using a 7.0 tesla MRI scanner (Magnet: Kobelco and Jastec, Japan; Console: Bruker Biospin, Germany) with a 35 mm diameter volume coil (Rapid biomedical GmbH, Rimpar, Germany). Transverse T_1-weighted two-dimensional images were obtained using a rapid acquisition with relaxation enhancement (RARE) sequence with the following parameters: repetition time = 600 ms; echo time = 9.57 ms; field of view = 38.4×38.4 mm^2; matrix = 256×256; slice thickness = 1.0 mm; RARE factor = 8 and the number of averages = 4. The spatial resolution was 0.15 mm $\times$ 0.15 mm $\times$ 1.0 mm. The total number of slices was 72, which covered from the base of the tail to the head. The polyethylene tube in the lower body fixture was filled with distilled water. To maintain vital heat, skin temperature around the chest region was measured using a fiber-optic thermometer (FOT-H,

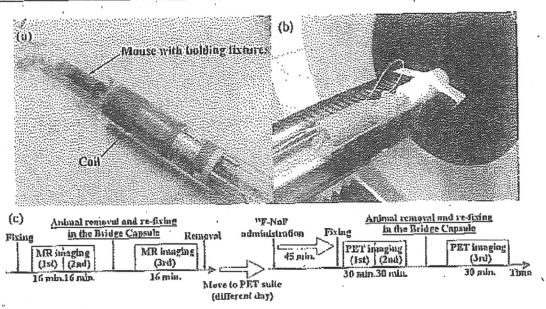

Figure 4. Setting for (a) MR and (b) PET imaging and (c) imaging protocol.

FISO Technology Inc., Quebec, Canada). Body temperature was maintained at approximately 36.0 ± 0.5 °C by an automatic heating system using warm air during the scans. The scan time was 15.36 min.

PET images were scanned using an Inveon Dedicated PET Scanner. The mouse under 2.0% isoflurane anesthesia was administered 7.4 MBq of ^{18}F-sodium fluoride (^{18}F-NaF) in a 100 μl via intravenous injection (Blau *et al* 1962, Even-Sapir 2005, Constantinescu and Mukherjee 2009); 0.74 MBq of ^{18}F-NaF was put into the polyethylene tube. After administration, the mouse was awakened for 45 min in order to realize sufficient uptake of ^{18}F-NaF into bone. The scan time was 30 min without an attenuation correction. All images were reconstructed with a maximum *a posteriori* (MAP) algorithm in a 128 × 128 × 159 matrix with a voxel size of 0.79 mm^3 and the following reconstruction parameters: MAP iteration = 18 and β factor = 0.

2.5. *Validation of reproducibility for the lower body*

The performance of the proposed system was validated using the positional discrepancies of the center of mass of the spinal column and the iliac bodies between corresponding images. These organs were chosen for the validation because small physiological movement was expected during the experiments in comparison with other soft tissues. The comparison ranges for this validation were approximately 15 mm at the spinal column and approximately 5 mm at both iliac bodies; there ranges are shown in figure 5(a). For the MR images, the positions of the center of mass at the spinal column and both sides of the iliac bodies were acquired using the differences in the signal intensities between the bones and marrow (figure 5(b)). For the PET images, the positions were acquired by bone imaging with ^{18}F-NaF. For the case of the comparing images between different modalities, the spatial resolutions of PET images were transferred to those of MR images; the position of the tuber coxae (figure 5(a)) in both images was chosen as the criterion position. The differences of the positions of the center of mass of the spinal column and both sides of the iliac bodies were calculated from the images after registration. The registration and accuracy validation were done using programs written in the MATLAB software (The MathWorks, MA, USA).

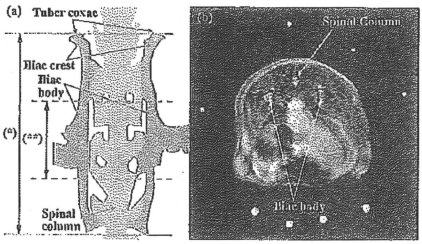

Figure 5. (a) Illustration of the bone structure in mouse lower body. The range between the solid lines (*) was used for validating the position accuracy in the spinal column, and the range between the dashed lines (**) was used for validating the position accuracy in both iliac bodies. (b) Example of the spinal column and iliac body on an MR image. The positions of the center of mass of the spinal column and both iliac bodies could be obtained by using the proposed image processing.

Table 1. Average differences (mm) in the positions of center of mass of the spinal column and iliac bodies ($N = 5$). The unit distance was 1 mm. 'Stability' denotes the average difference and standard deviation of the initial fixation to confirm the stability of the bridge capsule. 'Reproducibility' denotes the average difference and standard deviation of subsequent re-fixation to assess the reproducibility accuracy of after re-fixation.

	MRI–MRI		PET–PET		PET–MRI
	Stability	Reproducibility	Stability	Reproducibility	Reproducibility
Spinal column	0.17 ± 0.01	0.78 ± 0.22	0.16 ± 0.02	1.02 ± 0.21	1.80 ± 0.37
Iliac body (left)	0.20 ± 0.04	0.71 ± 0.32	0.23 ± 0.04	1.08 ± 0.22	1.66 ± 0.76
Iliac body (right)	0.18 ± 0.07	0.64 ± 0.38	0.21 ± 0.06	1.11 ± 0.25	1.64 ± 0.91

3. Results

Figure 6 shows typical MR and PET images using the proposed system. On the MR images, morphological structures, such as the kidneys and liver, were clearly visible. Artifacts caused by the proposed system, such as strain or image degradation, were not observed. The markers that were located around the lower body could be clearly seen. On the PET images, bone structures were visualized without any artifacts caused by the system. The markers over and under the mice were visualized well and had no influence on the PET images. Figure 7 shows a typical superimposed image using PET and MR images before and after image registration. The positions of the fiducial markers for the PET and MR images after registration were nearly the same.

Table 1 shows the average difference between before and after re-fixation for the spinal column and both iliac bodies ($N = 5$). The spinal column was distributed across 15 slices on MRI and 24 slices on PET, and the iliac body was distributed across 5 slices on MRI and 7 slices on PET. The average difference of reproducibility for the lower body before and after re-fixation was less than 0.78 mm in the MRI images and 1.11 mm in PET images, and less than 1.80 mm for the cross-modality registration. In one case, the positions of the fiducial markers in the lower body fixture barely moved in the in-plane directions, and it was difficult

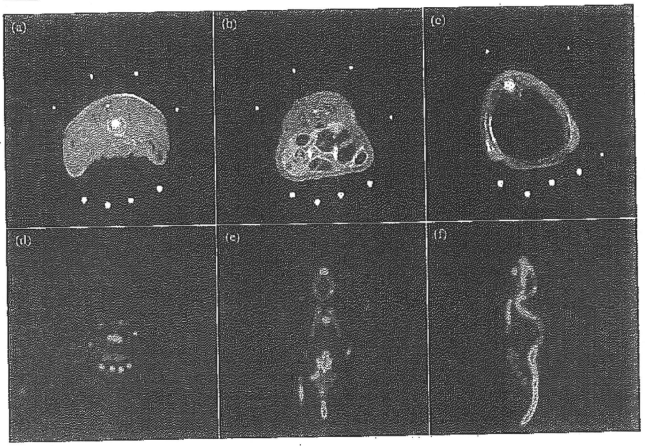

Figure 6. (a)–(c) MR and (d)–(f) PET images. In the MR images, the positions (a) and (b) were within the range covered by the lower body fixture, and (c) outside the fixture. On the PET images, the planes were (d) transverse, (e) horizontal and (f) saggital. No artifact was observed due to the proposed fixtures, and all fiducial markers were detectable in (a), (b) and (d).

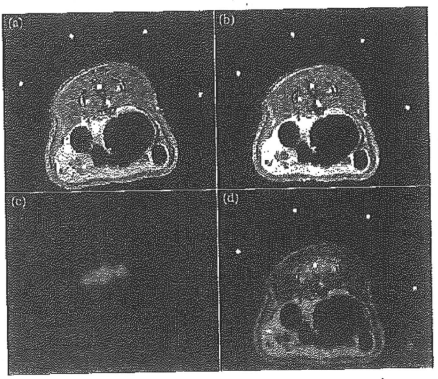

Figure 7. Typical superimposed image using MR and PET images. MR images (a) before and (b) after registration, (c) PET image and (d) superimposed image between MR and PET images after registration. The signals from a PET image at the spinal column and iliac bodies closely conformed to the signal from MR images. PET data are shown in color.

to distinguish the positions of the fiducial markers on several consecutive images. Therefore, these data were excluded from further evaluation of registration accuracy. In order to avoid registration errors, the tube should be embedded to present a more regular distribution of markers in the images.

4. Discussion and conclusion

In this study, a novel animal holding system, a 'bridge capsule', was proposed. This included specially designed holding fixtures that enabled small animal re-fixation with the same posture for longitudinal multimodal imaging experiments. Validation of positional reproducibility for the lower body was performed.

The bridge capsule system has separate head and lower fixtures. With the head part, the head of the mouse is fixed in position by gripping the skull and also the incisors with a movable part. The incisors could be easily gripped because the movable part could be manipulated with an internal spring to expose the hook. The size of this head fixture was adjustable and could be fit to the diameter of the volume coil used in this study. The size can be made smaller as per the coil size. At the lower body part, a mouse was fixed in place using a rubber-like fixture made from vinyl-silicone and a holder for the legs and tail. The advantages of using rubber-like materials like vinyl-silicone are that the holding fixture can be contoured to body shapes, maintains similar postures across rodents for longitudinal imaging experiments and can be attached and removed without changing the postures. Unexpected movement during imaging could be prevented by fitting the rubber-like fixture. The rubber-like material was easy to handle and did not exchange heat with the mice. Some attenuation could be attributed to the vinyl-silicone, but this problem can be avoided by performing a transmission scan for the PET experiments.

Regarding the image quality for MRI and PET using the proposed fixtures, no artifacts were observed, as shown in figure 6, although these fixtures were sources of attenuation and scatter. PET image quality could be improved by optimizing the parameters for MAP reconstruction and performing the attenuation correction. The positional differences between fixation and re-fixation for the spinal column and iliac bodies for the same modality were less than 0.8 mm on the MR images and 1.1 mm on PET images, and the average difference between fixation and re-fixation on the MRI and PET images was approximately 1.8 mm (table 1). The latter value was slightly larger than the values of the effective spatial resolutions of PET, which were shown to be 1.46 mm, 1.49 mm and 1.15 mm (Constantinescu and Mukherjee 2009). Therefore, the proposed fixtures could be used for re-fixation within 1.5 voxels of the reproducibility errors for multimodal imaging experiments. In such a case, the objective area still overlapped on the superimposed image after registration as shown in figure 7(d). Thus, an error of 1–2 voxels is probably not vital for our procedure. On the MR images, the spatial resolution in the z-direction was 1.0 mm, which was larger than that in the other directions. The average positional differences for MR images might be reduced by using thinner slices or three-dimensional acquisitions.

Regarding the holding fixtures, Rowland *et al* (2005) proposed another type of fixation that inserted ear bars into rodent ear holes from the side. Our head fixture was more compact and easier to use in comparison with this fixture because our fixtures used no ear bars or pillars to support the bars. The small size of the head fixture was suitable for MRI because a smaller volume coil provides higher sensitivity for MR imaging. In addition, the risk of injury to an eardrum or other parts using our fixture was less than that using an ear bar. For the lower body, a holding fixture made from a rubber-like material has been proposed for rat experiments by Rommel *et al* (2008). Our lower body fixtures are also more practical than

that fixture because our fixture was easy for re-fixation. The bridge capsule system fixed the lower body in place with cooperation between the rubber-like material and holder for the legs and tail. When re-fixing a rodent in place, the lower body fixture had to separate in order to remove the rodent's body and hind paws. This meant that the lower body fixtures were easy to remove and re-fix using the holder for legs and tail. Also, the head and lower body were immobilized, and the distance between these holding fixtures was kept constant by the bridge capsule system. Therefore, a mouse's posture outside of the fixation range using our fixtures, which was determined by the head and the lower body fixtures, was more similar to that before re-fixation than for the fixture used by Rommel *et al.*

The reproducibility accuracy of the lower body before and after re-fixation using the same modality was less than 0.78 mm in the MRI images and 1.11 mm in the PET images. These values were similar to previous studies where the differences were 1.11 mm for micro CT and less than 0.8 mm for micro PET (Zhang *et al* 2008, Suckow *et al* 2009). Suckow *et al* demonstrated registration of CT and PET images, but no previous results for the reproducibility accuracy have been shown when using different modalities. The average differences between MRI and PET shown in table 1 were larger than those before and after re-fixation using the same modality. The sources of these differences are thought to be causally related to the re-fixation, subtle changes in the abdominal organs, the low spatial resolution of PET and other incompatibilities between different imaging modalities. In previous works in the case of cross-modality imaging without re-fixation, the positions of the point markers implanted into tumors changed by approximately 0.5 mm between micro PET and MRI and approximately 0.2 mm between micro PET and micro CT (Zhang *et al* 2008, Suckow *et al* 2009). That discrepancy was probably due to the different characteristics of the different modalities. The increased positional differences for PET-MRI registration in our results probably originate from the same source.

As pointed out in previous research that used rubber-like material (Rommel *et al* 2008), these fixtures cannot immobilize internal organs, such as the liver, and displacements were unavoidable due to organ movement, tumor growth and disease state. The bridge capsule system also suffers from these factors. In order to adapt our fixture system for tumor growth, the lower body can be immobilized only where there are no tumor lesions.

In conclusion, we have proposed a bridge capsule system by which rodents can be re-fixed in place with practicable reposition reproducibility. This system enabled multimodal imaging and permitted a flexible design for experimental protocols. The system had two holding fixtures at the head and the lower body and these components provided good positional reproducibility. The proposed fixtures could be fixed and re-fixed for the same animal posture, and had no negative effects on image quality for MRI and PET. The difference of reproducibility before and after re-fixation using the same modality was less than approximately 0.8 mm and between different modalities was approximately 1.8 mm. We conclude that the bridge capsule system will become a useful device for multimodal imaging. This proposed system would be useful for longitudinal, repeated and multimodal imaging experiments that require highly reproducible animal posture.

Acknowledgments

The authors thank Mr Takeo Shimomura for making the head fixture, Miss Sayaka Shibata, Miss Ric Hirano and Mr Teppei Nakahara for MR imaging experiments, Mr Hidekatsu Wakizaka for PET imaging experiments, and the staff of the Cyclotron Operation and Radiopharmaceutical Production sections for the cyclotron operation and production of radioisotopes. They also thank Mr Jeff Kershaw for helpful advice and assistance.

References

Blau M, Nagler W and Bender M A 1962 Fluorine-18: a new isotope for bone scanning *J. Nucl. Med.* 3 332–4

Catana C, Wu Y, Judenhofer M S, Qi J, Pichler B J and Cherry S R 2006 Simultaneous acquisition of multislice PET and MR images: initial results with a MR-compatible PET scanner *J. Nucl. Med.* 47 1968–76

Chow P L, Stout D B, Komisopoulou E and Chatziioannou A F 2006 A method of image registration for small animal, multi-modality imaging *Phys. Med. Biol.* 51 379–90

Christian N, Lee J A, Bol A, De Bast M, Gallez B and Gregoire V 2008 Immobilization device for *in vivo* and *in vitro* multimodality image registration of rodent tumors *Radiother. Oncol.* 87 147–51

Constantinescu C C and Mukherjee J 2009 Performance evaluation of an Inveon PET preclinical scanner *Phys. Med. Biol.* 54 2885–99

Even-Sapir E 2005 Imaging of malignant bone involvement by morphologic, scintigraphic, and hybrid modalities *J. Nucl. Med.* 46 1356–67

Gilbert K M, Handler W B, Scholl T J, Odegaard J W and Chronik B A 2006 Design of field-cycled magnetic resonance systems for small animal imaging *Phys. Med. Biol.* 51 2825–41

Handler W B, Gilbert K M, Peng H and Chronik B A 2006 Simulation of scattering and attenuation of 511 keV photons in a combined PET/field-cycled MRI system *Phys. Med. Biol.* 51 2479–91

Humm J L *et al* 2003 A stereotactic method for the three-dimensional registration of multi-modality biologic images in animals: NMR, PET, histology, and autoradiography *Med. Phys.* 30 2303–14

Judenhofer M S, Catana C, Swann B K, Siegel S B, Jung W I, Nutt R E, Cherry S R, Claussen C D and Pichler B J 2007 PET/MR images acquired with a compact MR-compatible PET detector in a 7-T magnet *Radiology* 244 807–14

Luker G D and Piwnica-Worms D 2001 Molecular imaging *in vivo* with PET and SPECT *Acad. Radiol.* 8 4–14

Massoud T F and Gambhir S S 2003 Molecular imaging in living subjects: seeing fundamental biological processes in a new light *Genes Dev.* 17 545–80

Pichler B J, Judenhofer M S, Catana C, Walton J H, Kneilling M, Nutt R E, Siegel S B, Claussen C D and Cherry S R 2006 Performance test of an LSO-APD detector in a 7-T MRI scanner for simultaneous PET/MRI *J. Nucl. Med.* 47 639–47

Pichler B J, Wehrl H F and Judenhofer M S 2008 Latest advances in molecular imaging instrumentation *J. Nucl. Med.* 49 Suppl 2 5S–23S

Rommel D, Abarca-Quinones J, Christian N, Peeters F, Lonneux M, Labar D, Bol A, Gregoire V and Duprez T 2008 Alginate moulding: an empirical method for magnetic resonance imaging/positron emission tomography co-registration in a tumor rat model *Nucl. Med. Biol.* 35 571–7

Rowland D J, Garbow J R, Laforest R and Snyder A Z 2005 Registration of [18F]FDG microPET and small-animal MRI *Nucl. Med. Biol.* 32 567–72

Suckow C, Kuntner C, Chow P, Silverman R, Chatziioannou A and Stout D 2009 Multimodality rodent imaging chambers for use under barrier conditions with gas anesthesia *Mol. Imaging Biol.* 11 100–6

Weissleder R and Mahmood U 2001 Molecular imaging *Radiology* 219 316–33

Woo S K, Kim K M, Lee T S, Jung J H, Kim J G, Kim J S, Choi T H, An G I and Cheon G J 2009 Registration method for the detection of tumors in lung and liver using multimodal small animal imaging *IEEE Trans. Nucl. Sci.* 56 1454–8

Yamamoto S, Imaizumi M, Kanai Y, Tatsumi M, Aoki M, Suglyama E, Kawakami M, Shimosegawa E and Hatazawa J 2010 Design and performance from an integrated PET/MRI system for small animals *Ann. Nucl. Med.* 24 89–98

Zanzonico P, Campa J, Polycarpe-Holman D, Forster G, Finn R, Larson S, Humm J and Ling C 2006 Animal-specific positioning molds for registration of repeat imaging studies: comparative microPET imaging of F18-labeled fluoro-deoxyglucose and fluoro-misonidazole in rodent tumors *Nucl. Med. Biol.* 33 65–70

Zhang M, Huang M, Le C, Zanzonico P B, Claus F, Kolbert K S, Martin K, Ling C C, Koutcher J A and Humm J L 2008 Accuracy and reproducibility of tumor positioning during prolonged and multi-modality animal imaging studies *Phys. Med. Biol.* 53 5867–82

Intracortical Microcirculatory Change Induced by Anesthesia in Rat Somatosensory Cortex

Kazuto Masamoto, Takayuki Obata, and Iwao Kanno

Abstract The present study aimed to characterize microcirculatory responses to anesthesia in brain tissue. With multi-photon excitation fluorescence microscopy, intra-cortical capillary dimension and red blood cell (RBC) flow were successfully visualized up to a depth of ~0.6 mm from the cortical surface in rats anesthetized with either isoflurane or α-chloralose. We observed that the diameter of the major cerebral artery was ~100 μm under isoflurane, but ~75 μm under α-chloralose. The capillary diameter was observed to be larger under α-chloralose than isoflurane: 5.1 ± 1.2 μm vs. 4.8 ± 1.1 μm, respectively. A significant difference in the mean RBC speed measured in single capillaries was observed: 0.4 ± 0.4 mm/s under α-chloralose vs. 1.5 ± 0.4 mm/s under isoflurane. In agreement with these observations, arterio-venous transit-time and laser-Doppler flowmetry consistently showed a significant reduction of the RBC and plasma blood speed under α-chloralose relative to isoflurane. These findings may indicate that local blood flow regulatory mechanisms exist at the capillary level for the balance of oxygen supply and demand induced by anesthesia in the brain tissue.

1 Introduction

A variety of brain tissue oxygen levels have been observed in animals under general anesthesia [1]. The direct and indirect effects of anesthesia involve the degree of anesthetic action on cerebral metabolic rate of oxygen (CMR_{O2}) and cerebral blood flow (CBF).

In a previous study, we found that rodents treated with inhalation anesthetics (e.g., isoflurane) or intravenous anesthetics (e.g., α-chloralose) that are widely used for brain activation studies, showed quite different behaviors for

K. Masamoto (✉)
Molecular Imaging Center, National Institute of Radiological Sciences, Chiba, 263-8555, Japan
e-mail: masamoto@nirs.go.jp

E. Takahashi, D.F. Bruley (eds.), *Oxygen Transport to Tissue XXXI*, Advances in Experimental Medicine and Biology 662,
DOI 10.1007/978-1-4419-1241-1_7,

the activation-induced cortical hemodynamics [2]. Since hemodynamic-based brain imaging techniques rely on the microcirculatory responses to local neural activity, the effects of anesthesia on the brain microcirculation are critically important for interpretation of the imaging signals. However, the effects of anesthesia on the brain microcirculation, such as vessel dimension and red blood cell (RBC) flow remain unaddressed.

In the present study, we directly measured intracortical capillary dimension and RBC flow in the cerebral cortex of rats anesthetized with either volatile isoflurane or injectable α-chloralose. A biocompatible fluorescent dye was intravenously injected for visualization of blood plasma and cortical microvasculature was three-dimensionally visualized with in vivo multi-photon excitation fluorescent microscopy up to a depth of 0.6 mm from the cortical surface. Intraluminal vascular dimension and fluorescently labeled RBC speed were then measured.

2 Materials and Methods

All animal protocols were approved by the NIRS Animal Experiment Committee. The animals (250–350 g Sprague-Dawley rats, $N=9$) were initially anesthetized with 4–5% isoflurane and maintained with 2% during surgical procedures. The animal was mechanically ventilated and physiologic parameters (e.g., end-tidal CO_2, anesthetic gas concentration, respiratory rate, heart rate, and mean arterial blood pressure) were monitored throughout all experiments. Arterial blood gas was periodically measured, and respiratory rate and minute ventilation volume were adjusted as needed. Rectal temperature was maintained at 37.0 ± 0.2°C.

A portion of the left skull (3 mm by 3 mm) over the somatosensory area was removed. The opened area was filled with physiologic saline solution. For experiments, the anesthesia level was first maintained with isoflurane (~1.4%) and then switched to α-chloralose (45 mg/kg/h, i.v.), as previously reported [2]. For visualization of the cortical vasculature, a bolus of Qdot® 605 (1 μM in buffered solution, Invitrogen) was intravenously injected (0.2–0.4 ml). The cortical vasculature was then visualized with multi-photon excitation fluorescent microscope (TCS SP5, Leica Microsystems) with an excitation wavelength of 900 nm (Mai-Tai, Ti:Sapphire laser, Spectra-Physics). The objective lens was a 20× water-immersion lens (0.5 NA, Leica Microsystems). The 512 pixel by 512 pixel images covered a cortical area of 456 μm by 456 μm with a pixel resolution of 0.89 μm. To obtain the three-dimensional structure, contiguous images were captured up to a depth of 0.6 mm from the cortical surface with a step size of 0.01 mm in the z-direction. The region of interest was selected with care to avoid areas having vessels of a relatively large size at the cortical surface. A final image was taken to cover an area of 912 μm by 912 μm in the x-y plane by scanning four adjacent regions. For display purposes, a maximum-intensity projection was constructed from contiguous images obtained in the z-direction.

Based on their pulsation and branching geometry, arterial and venous networks were distinguished at the cortical surface, and then tracked into the parenchyma tissue. To measure capillary diameter, a maximum intensity projection was created from every 0.1-mm thickness in the z-direction and then the width in the image was calculated. A single capillary was defined as the single vessel having cross-sectional thickness less than 8 μm and for which both edges continued to two new vessels as a branching.

The RBC speed was measured by tracking a FITC-labeled RBC through a single capillary. Time-lapse images were obtained at a rate of 14–167 frames per second, depending on the number of lines to be scanned in each single frame. The scanning area was set to cover the whole structure of the single-capillary shape (i.e., 64–256 lines). Similarly, the speed of blood plasma was evaluated by tracking 0.1-μm diameter fluorescent beads that were intravenously injected. For the measurement of mean arterio-venous transit time, a bolus injection (0.1 ml) of fluorescently labeled RBCs or fluorescent beads was performed via the femoral vein. The time-lapse image was obtained with a 5× objective lens at a rate of seven frames per second. Statistical significance was determined with a t-test ($P < 0.05$).

3 Results

There was no detectable difference in the measured physiologic parameters (arterial blood gas and blood pressure) between isoflurane and α-chloralose conditions (Table 1). We observed that the diameter of the principal artery at the cortical surface was ~100 μm under isoflurane, but ~75 μm under α-chloralose. The results showed that the principal artery shrank significantly after induction with α-chloralose. However, the intracortical capillary diameter was slightly larger under α-chloralose (5.1 ± 1.2 μm, $n = 1682$ vessels) compared to the isoflurane condition (4.8 ± 1.1 μm, $n = 1746$ vessels). A statistically significant difference was observed between two conditions. These results indicate that the upstream and downstream vessels react differently depending on the anesthetics.

Table 1 Blood gas conditions, mean arterial blood pressure (BP), and mean capillary diameter (Dc) observed under isoflurane (Iso) and α-chloralose (Acl) conditions (Mean ± SD, $N = 9$). *$P < 0.05$ (Iso vs. Acl)

	pH	pCO_2 (mmHg)	pO_2 (mmHg)	BP (mmHg)	Dc (μm)
Iso	7.43 ± 0.03	37 ± 3	128 ± 18	94 ± 11	4.8 ± 1.1
Acl	7.44 ± 0.02	36 ± 2	123 ± 16	115 ± 15	5.1 ± 1.2*

The mean RBC speed in a single capillary was significantly lower under α-chloralose relative to the isoflurane condition: 0.4 ± 0.4 mm/s under α-chloralose vs. 1.5 ± 0.4 mm/s under isoflurane. Under α-chloralose, some RBCs were found

to be very slow (<0.01 mm/s), whereas most RBCs measured under isoflurane had a relatively high speed (0.4–3.0 mm/s).

As expected, the arterio-venous transit-time of the labeled RBCs was significantly longer under α-chloralose (2.8 ± 1.7 s at peak-to-peak) as compared to the isoflurane condition (1.0 ± 0.9 s). Similar results were observed for the transit time of blood plasma: 1.8 ± 1.3 s under α-chloralose and 1.2 ± 0.7 s under isoflurane. These results indicated that the both RBC and plasma blood speed were significantly lower under α-chloralose relative to isoflurane conditions.

4 Discussion

It has been previously shown by other groups that the baseline CBF under α-chloralose was 30–50% lower than under isoflurane in rat somatosensory cortex, i.e. 70–90 mL/100 g/min under α-chloralose [3, 4] vs. 130–150 mL/100 g/min under isoflurane [5, 6]. In a previous study, we found the baseline CBF measured with laser-Doppler flowmetry was 31% lower under α-chloralose compared with isoflurane [2]. Our measurements of the arterial dimension are in good agreement with these literature data, indicating that the tone in the upstream resistance vessels has a significant role in the regulatory mechanism of the baseline CBF induced by anesthesia. However, we also found that the effect of the anesthesia on the intracortical capillary diameter was opposite to the arterial response. Namely, a larger capillary diameter was observed under α-chloralose as compared to the isoflurane condition. This might indicate that the upstream arteries and intracortical microvessels have separate or independent mechanisms for the regulation of local CBF.

Our results for the mean RBC speed consistently showed that the speed was significantly lower under α-chloralose relative to the isoflurane condition. The results are consistent with previous CBF data. However, the measured RBC speed under isoflurane was relatively high. Kleinfeld et al. (1998) reported that the intra-cortical RBC speed was 0.77 mm/s in rats anesthetized with urethane [7]. The ranges of RBC speed in capillaries were reported as 0.3–3.2 mm/s [8]. In the present study, we showed that the variable speed of RBCs could be due to a local regulatory mechanism rather than upstream arterial regulation. Since the capillary volume and speed of RBCs critically affect oxygen transfer processes from nearby blood vessels to the energy consuming tissue site, it is worthwhile to compare the tissue oxygen level between both anesthesia conditions. Our group has reported that the mean tissue oxygen level in rat somatosensory cortex was 29 mmHg under α-chloralose and 33 mmHg under isoflurane [9, 10]. Another study with electron paramagnetic resonance oximetry showed that the mean tissue oxygen level at normoxic conditions was 13 mmHg under a cocktail of α-chloralose and urethane and 38 mmHg under isoflurane [11]. The data from those studies were in good agreement with the CBF data; higher CBF produces higher tissue oxygen and vice versa. The anesthesia may also affect the tissue oxygen metabolic rate in a different manner, and thus a possible scenario

where the effect of anesthesia on the energy metabolism becomes a dominant factor leading to the observed difference in tissue oxygen level cannot be ruled out. However, it should be noted that endothelial cells have the ability to control their dimension by sensing the nearby blood oxygenation level [12], which may play a role in adjusting local oxygen demand and supply via regulation of capillary volume and RBC speed. Further studies are needed to elucidate the full regulatory mechanism for the local regulation of the microvascular dimensions and RBC traffic.

Acknowledgments This work was partially supported by KAKENHI (#19800065).

References

1. Ndubuizu, O., LaManna, J. C., 2007, Brain tissue oxygen concentration measurements, Antioxid Redox Signal. 9:1207–1219.
2. Masamoto, K., Kim, T., Fukuda, M., Wang, P., Kim, S. G., 2007, Relationship between neural, vascular, and BOLD signals in isoflurane-anesthetized rat somatosensory cortex, Cereb Cortex. 17:942–950.
3. Ueki, M., Linn, F., Hossmann, K. A., 1988, Functional activation of cerebral blood flow and metabolism before and after global ischemia of rat brain, J Cereb Blood Flow Metab. 8:486–494.
4. Lee, S. P., Duong, T. Q., Yang, G., Iadecola, C., Kim, S. G., 2001, Relative changes of cerebral arterial and venous blood volumes during increased cerebral blood flow: implications for BOLD fMRI, Magn Reson Med. 45:791–800.
5. Maekawa, T., Tommasino, C., Shapiro, H. M., Keifer-Goodman, J., Kohlenberger, R. W., 1986, Local cerebral blood flow and glucose utilization during isoflurane anesthesia in the rat, Anesthesiology. 65:144–151.
6. Lenz, C., Frietsch, T., Futterer, C., Rebel, A., van Ackern, K., Kuschinsky, W., Waschke, K. F., 1999, Local coupling of cerebral blood flow to cerebral glucose metabolism during inhalational anesthesia in rats: desflurane versus isoflurane, Anesthesiology. 91:1720–1723.
7. Kleinfeld, D., Mitra, P. P., Helmchen, F., Denk, W., 1998, Fluctuations and stimulus-induced changes in blood flow observed in individual capillaries in layers 2 through 4 of rat neocortex, Proc Natl Acad Sci U S A. 95:15741–15746.
8. Hudetz, A. G., 1997, Blood flow in the cerebral capillary network: a review emphasizing observations with intravital microscopy, Microcirculation. 4:233–252.
9. Masamoto, K., Kershaw, J., Ureshi, M., Takizawa, N., Kobayashi, H., Tanishita, K., Kanno, I., 2007, Apparent diffusion time of oxygen from blood to tissue in rat cerebral cortex: implication for tissue oxygen dynamics during brain functions, J Appl Physiol. 103:1352–1358.
10. Masamoto, K., Vazquez, A., Wang, P., Kim, S. G., 2008, Trial-by-trial relationship between neural activity, oxygen consumption, and blood flow responses, Neuroimage. 40:442–450.
11. Hou, H., Grinberg, O. Y., Taie, S., Leichtweis, S., Miyake, M., Grinberg, S., Xie, H., Csete, M., Swartz, H. M., 2003, Electron paramagnetic resonance assessment of brain tissue oxygen tension in anesthetized rats, Anesth Analg. 96:1467–1472.
12. Inoue, K., Tomita, M., Fukuuchi, Y., Tanahashi, N., Kobari, M., Takao, M., Takeda, H., Yokoyama, M., 2003, Dynamic observation of oxygenation-induced contraction of and transient fiber-network formation-disassembly in cultured human brain microvascular endothelial cells, J Cereb Blood Flow Metab. 23:821–828.

Ann Nucl Med (2010) 24:249–260
DOI 10.1007/s12149-010-0364-z

ORIGINAL ARTICLE

Quantitative analysis of dopamine transporters in human brain using [^{11}C]PE2I and positron emission tomography: evaluation of reference tissue models

Chie Seki · Hiroshi Ito · Tetsuya Ichimiya · Ryosuke Arakawa · Yoko Ikoma · Miho Shidahara · Jun Maeda · Akihiro Takano · Hidehiko Takahashi · Yuichi Kimura · Kazutoshi Suzuki · Iwao Kanno · Tetsuya Suhara

Received: 25 August 2009 / Accepted: 13 January 2010 / Published online: 3 April 2010

Abstract
Objective Dopamine transporter (DAT) is a reuptake carrier of dopamine at presynapse that regulates dopaminergic neural transmission. [^{11}C]PE2I is a cocaine analog developed as a potent positron emission tomography (PET) ligand for DAT with high selectivity. The aim of this study was to evaluate the applicability of quantification methods using reference tissue models for [^{11}C]PE2I.
Methods Dynamic PET scans were performed in 6 young healthy male volunteers after an intravenous bolus injection of [^{11}C]PE2I. Metabolite-corrected arterial plasma-input functions were obtained. Compartment model analysis and plasma-input Logan analysis were performed to determine the kinetic parameters and distribution volume (V_T). The distribution volume ratio (*DVR*) was calculated as the ratio of V_T in the cerebral region to that in the cerebellum. *DVR*s were also determined by the original multilinear reference tissue model method (MRTMo) and the simplified reference tissue model method (SRTM), comparing the results with those obtained from graphical analysis using arterial input function. To estimate errors in *DVR* calculated using the reference tissue model, a simulation study that focused on cerebellar kinetics and scan duration was performed.
Results The highest [^{11}C]PE2I binding was observed in the striatum, followed by the midbrain and thalamus. The 2-tissue model was preferable to the 1-tissue model for describing the [^{11}C]PE2I kinetics in the cerebellum. Both the measured and 90-min simulated data showed that reference tissue models caused an underestimation of *DVR* in the striatum. The simulation showed that 90-min scan duration was insufficient when cerebellar kinetics was described as a 1-tissue model. Nevertheless, *DVR* values determined by MRTMo and SRTM were in good agreement with those by the graphical approach in other lower binding regions.
Conclusion Due to the [^{11}C]PE2I kinetics in the cerebellum and limited scan duration for ^{11}C, MRTMo and SRTM underestimated the striatal *DVR*. Despite this limitation, the present study demonstrated the applicability of reference tissue models. Since DAT in the midbrain and thalamus is of interest in the pathophysiology of neuropsychiatric disease, this noninvasive quantitative analysis will be useful for clinical investigations.

Keywords [^{11}C]PE2I · Human · Kinetic modeling · Positron emission tomography (PET) · Reference tissue model

C. Seki · H. Ito (✉) · T. Ichimiya · R. Arakawa · Y. Ikoma · M. Shidahara · J. Maeda · A. Takano · H. Takahashi · Y. Kimura · K. Suzuki · I. Kanno · T. Suhara
Molecular Imaging Center, National Institute of Radiological Sciences, 4-9-1 Anagawa, Inage-ku, Chiba 263-8555, Japan
e-mail: hito@nirs.go.jp

Introduction

Dopaminergic neurotransmission is of interest in the pathophysiology of neuropsychiatric disease. One of the presynaptic functions is the dopamine reuptake mediated by dopamine transporter (DAT), a membrane-bound protein. A number of radioligands for in vivo DAT imaging have been developed for positron emission tomography (PET), such as [^{11}C]cocaine [1], [^{11}C]WIN35,428 (CFT) [2, 3], [^{11}C]β-CIT (RTI-55) [4], [^{11}C] β-CIT-FE [5], [^{11}C]D-threo-methylphenidate [6], [^{18}F]FECNT [7], [^{11}C]Altropane [8], [^{11}C]PE2I [9] and most recently [^{11}C]LBT-999 [10]. Most of them are analogs of cocaine

and have some degree of affinity for the serotonin transporter. The tropane analog *N*-(3-iodoprop-2E-enyl)-2β-carbomethoxy-3β-(4-methylphenyl) nortropane (PE2I) has 29-fold higher affinity for DAT than for serotonin transporter and more than 58-fold higher affinity than for noradrenalin transporter [9]. Thus, ^{11}C-labeled PE2I, [^{11}C]PE2I(([^{11}C]-(E)-*N*-3-isodoprop-2-ethyl)-2β-carbomethoxy-3β-(4-methylphenyl)nortropane), can be expected to represent a selective PET radioligand for the evaluation of DAT.

Previous reports have demonstrated the successful visualization of brain DAT by [^{11}C]PE2I and PET in human and nonhuman primates [11, 12]. Changes in DAT binding in Parkinson's disease, attention-deficit/hyperactivity disorder (ADHD) and schizophrenia have also been observed using [^{123}I]PE2I [13, 14] and [^{11}C]PE2I [15–17], respectively. Quantitative analysis using both arterial input function and reference tissue in humans has been reported with [^{123}I]PE2I [18, 19] and [^{11}C]PE2I [20–22]. It has been reported that the binding potential (BP_{ND}) values of striatal regions are underestimated by the simplified reference tissue model (SRTM) method [20, 23] compared with those by kinetic analysis and Logan analysis with use of arterial input function in [^{11}C]PE2I PET studies [20–22]. However, neither the cause of the underestimation with SRTM nor the applicability of SRTM to other brain regions has as yet been investigated in detail.

In this study, we attempted to validate quantification methods using a reference tissue model in [^{11}C]PE2I PET studies with both measured PET data and simulated data. In addition to SRTM, the original multilinear reference tissue model (MRTMo) [24] was applied to estimate the distribution volume ratio (*DVR*), instead of BP_{ND}, and compared by quantitative analysis using arterial input function.

Materials and methods

Calculation of specific binding

Specific binding of [^{11}C]PE2I to DAT can be evaluated by the tracer *DVR* of the target brain region to the reference tissue region showing negligible specific binding according to the following equation:

$$DVR = \frac{V_T}{V_T'} \tag{1}$$

where V_T and V_T' are the distribution volumes of the target brain and reference region, respectively. The distribution volume can be estimated using kinetic analysis and plasma-input Logan analysis with arterial input function.

Quantification using arterial input function

Kinetic analysis

To describe the [^{11}C]PE2I kinetics in the brain regions, the 2-tissue model consisting of plasma and two tissue components (2-tissue model) was used [22, 25–27]. In this model, the following equations are expressed:

$$C_T(t) = C_{ND}(t) + C_S(t), \tag{2}$$

$$\frac{dC_{ND}(t)}{dt} = K_1 C_p(t) - k_2 C_{ND}(t) - k_3 C_{ND}(t) + k_4 C_S(t), \tag{3}$$

$$\frac{dC_S(t)}{dt} = k_3 C_{ND}(t) - k_4 C_S(t). \tag{4}$$

C_T is the total radioactivity concentration in the brain tissue, C_{ND} is the radioactivity concentration of nondisplaceable radioligand in the brain tissue, which includes nonspecifically bound and free radioligand concentrations, C_S is the radioactivity concentration of the radioligand specifically bound to DAT, and C_p is the radioactivity concentration of the unchanged radioligand in plasma (arterial input function). The rate constants K_1 and k_2 describe the influx and efflux rates for radioligand diffusion through the blood–brain barrier (BBB), respectively. The rate constants k_3 and k_4 represent the radioligand transfer between the compartments for nondisplaceable radioligand and specific radioligand binding to receptors, respectively.

For the 1-tissue model, K_1 and k_2 are the influx and efflux rates for radioligand diffusion through BBB:

$$C_T(t) = C_{ND}(t), \tag{5}$$

$$\frac{dC_{ND}(t)}{dt} = K_1 C_p(t) - k_2 C_{ND}(t). \tag{6}$$

Total distribution volume (V_T) denotes the tracer concentration ratio of tissue to plasma under equilibrium condition. V_T is calculated for the 2-tissue model as follows:

$$V_T = \frac{K_1}{k_2}\left(1 + \frac{k_3}{k_4}\right). \tag{7}$$

For the 1-tissue model:

$$V_T = \frac{K_1}{k_2}. \tag{8}$$

Additionally, V_b (ml/ml) was introduced as the fractional volume of blood space in the region. Then measured radioactivity concentration of the region with PET is expressed as,

$$C_{ROI}(t) = V_b C_b(t) + (1 - V_b) C_T(t) \tag{9}$$